Spring 2022

Upper Regime Bedform Geometries and Types as a Function of Sediment Supply and Grain Size

Sydney Sanders

UPPER REGIME BEDFORM GEOMETRIES AND TYPES AS A FUNCTION OF SEDIMENT SUPPLY AND GRAIN SIZE

by

Sydney Sanders

Bachelor of Science in Civil Engineering
University of South Carolina, 2020

Submitted in Partial Fulfillment of the Requirements

For the Degree of Master of Science in

Civil and Environmental Engineering

College of Engineering and Computing

University of South Carolina

2022

Accepted by:

Enrica Viparelli, Director of Thesis

Shamia Hoque, Reader

Erfan Goharian, Reader

Tracey L. Weldon, Interim Vice Provost and Dean of the Graduate School

DEDICATION

To my late uncle Randy Feaster who exposed me to the field of engineering, to my family and friends who have shown unconditional love and support... and to myself for preserving throughout this chapter of life... I dedicate this to us.

ACKNOWLEDGEMENTS

The author displays great gratitude to her advisor Enrica Viparelli, who was not only an advisor but a phenomenal leader and mentor throughout both undergraduate and master studies. Also, extensive thanks to the lab group who put in countless hours to help prepare and run experiments: Ryan Johnson, Amanda Balkus, Mahsa Ahmadpoor, Brandon Fryson, and Briana McQueen. The author would also like to thank Sadegh Jafarinik and Ricardo Hernandez-Moreira for mentoring her as an undergraduate student and allowing her to advance their discoveries. This project is funded by EXXON Mobil.

ABSTRACT

Most research on fluvial bedforms focuses on the study of dunes (lower regime), and much less is known on upper regime bedforms. Studying upper regime bedforms, the conditions in which they form and how the geometry changes with flow and sediment properties is necessary for interpreting the stratigraphic record, estimate flow resistance and reconstruct flow characteristics from observed geometries. Here I present results of laboratory experiments designed to investigate the role of suspended bed material and sediment grain size on upper regime bedforms. Experiments were performed in open channel flow mode in a sediment-feed flume with a 0.19 m wide, 0.9 m deep, 7 m long test reach. Mean grain sizes ranged between 0.22 mm and 0.87 mm. All experiments started from a net-depositional or net-erosional (disequilibrium) condition and continued until the bed level averaged over a series of bedforms did not change in time (equilibrium). In a sediment feed flume at equilibrium, the total (bedload plus suspended load) bed material load is known because it must be equal to the sediment feed rate to guarantee mass conservation. Equilibrium water surface and bed level measurements were used to characterize average flow conditions, suspended sediment concentration was measured, and the near bed suspended sediment concentration was estimated. As expected, suspended bed material load significantly increased as the sediment grain size decreased. Our results confirm that as the ratio between the bed material load and the flow discharge increases, the bed configuration evolves from lower regime to upper regime. As the ratio between bed material load and flow discharge increases, upper

regime bedforms become longer (i.e., the wavelength increases) and the flow depth becomes shallower. In experiments with relatively coarse sand transported as bedload transport, we observed the transition from upstream migrating antidunes to plane bed with bedload transport in sheet flow mode. In experiments with significant suspended bed material load, we observed the transition from downstream migrating antidunes to upstream migrating antidunes, which tend to evolve toward cyclic steps as the ratio between sediment supply and water discharge increases.

TABLE OF CONTENTS

LIST OF TABLESS

LIST OF FIGURES

LIST OF SYMBOLS

σ_g	Standard deviation
Δ	Bedform height
λ	Wavelength
D_g	Geometric mean diameter
D_{sg}	Geometric diameter of the sediment on the bed surface
A_{cs}	Area of entire cross section
A_b	Cross sectional area of bed region
A_{wb}	Cross sectional area of wall region
B	Rectangular channel cross-section width of the flume
C_f	Non-dimensional friction coefficient
$C_{f_{cs}}$	Non-dimensional friction coefficient of entire cross section
C_{f_b}	Non-dimensional friction coefficient of bed region
C_{f_w}	Non-dimensional friction coefficient of wall region
g	Acceleration of gravity
P_{cs}	Wetted perimeter of entire cross section
P_b	Wetted perimeter of bed region
P_w	Wetted perimeter of wall region
Q_w	Water discharge

Q_z	Feed rate
H	Flow depth
r	Hydraulic radius
r_b	Hydraulic radius of the bed region
r_w	Hydraulic radius of wall region
Re_{cs}	Reynolds number for entire cross section
Re_b	Reynolds number for bed region
Re_w	Reynolds number for wall region
ν	Kinematic viscosity
f_w	Darcy- Weisbach friction coefficient
k_s	Roughness height
n_k	Constant equal to 2
τ^*_{sg}	Shields number due to skin friction
α_r	Constant equal to 8.1
u^*	Shear velocity
u^*_s	Shear velocity due to skin friction
U	Mean velocity
κ	Von Karman constant equal to 0.41
v_s	Settling velocity
c	Suspended sediment concentration
c_b	Computed suspended sediment concentration
z	Vertical coordinate with origin on the channel bed
z_b	Non-dimensional near bed reference elevation

H_o Flow depth due to skin friction

Fr_o Froude number due to skin friction

k Nondimensional wave number

CHAPTER 1

INTRODUCTION

Sediment transport, erosion, and deposition, as well as the formation and evolution of sediment waves, in alluvial systems are areas of research with a substantial amount of knowledge left to be discovered. Notwithstanding, the large body of studies on sediment transport and bedforms, the effects of sediment properties, flow characteristics and mode of sediment transport on sediment entrainment and deposition, as well as on bedform characteristics, remain poorly understood (for example, Araya & Masuda, 2001; Capart & Fraccarollo, 2011; Hernandez Moreira et. al, 2020).

Understanding sediment transport processes is important from both engineering and geological perspectives (Yokokawa et. al, 2019). From a civil engineering perspective, fluid mechanics and open channel flow hydraulics are utilized to determine relationships between flow discharge, flood water depths and bedform types observed in laboratory and field settings. These relationships are generally determined by calculating resistance factors (Alexander & Fielding, 1997; Froude et. al, 2017) and can be used to construct models that will aid in the advancement of flood prevention and safety. Geology wise, the stratigraphy (rock layers/ layering) left by migrating bedforms can further be examined to interpret the rock record and reconstruct paleo-flow (flow of fluids over geological time) characteristics with applications to hydrocarbon exploration

(Pickup, et. al, 1994; Smillie et. al, 2019). Further, the sediment within and surrounding hydrocarbon reservoirs may vary in hydraulic conductivity, which controls how easily a fluid can move through a porous material. Understanding how coarse and fine sediment particles are deposited can thus provide new knowledge for the development of drilling techniques and the placement of hydrocarbons within given geological regions (Smillie et. al, 2019). Reconstruction of paleo-flows can also provide answers or insight to historical questions on effects of vegetation and humans on water systems as they alter the sediment deposits (Vesipa, 2012; Yang & Nepf, 2019).

Sediment forms the beds of natural water bodies, ranging from small-scale ponds and lakes to large rivers and oceans (Alexander et. al, 2001). Sediment can be transported in two different modes: bedload or suspended load. Bedload transport is defined as the motion of sediment particles that move close to the bed surface in a sliding, rolling, or saltating mode. Suspended load refers to the sediment particles that are in motion within the water column, far away from the bed surface. Fluid properties, sediment size, and density control the transportation mode (Vanoni, 2006; Turowski et. al, 2010). It is important to note that bedload and suspended load transport can occur simultaneously. Exploratory experimental studies of sediment transport date back to the 1900s, and theoretical analysis to determine how bedforms form in respect to open-channel flows started in the 1950s (see for example Englund, 1970). One of the first and most complete set of experiments on fluvial bedforms was designed and performed in Fort Collins at Colorado State University (Guy et al., 1966).

Bed configurations and fluvial bedforms are generally classified in terms of two regimes: lower regime and upper regime (Kennedy, 1960; Simons & Richardson 1966;

Carling & Shvidchenko, 2002). Lower regime bed configurations consist of plane beds, and bedforms such as ripples and dunes. These bedforms migrate in the downstream direction. Lower regime plane bed occurs when sediment waves do not form, and it is typical of gravel bed rivers. Ripples and dunes occur in Froude subcritical conditions (Froude numbers less than 1).

Upper regime bed configurations and bedforms consist of upper regime plane bed and bedforms such as antidunes and cyclic steps, also referred to as chutes and pools, and occur with Froude numbers close or greater than 1 (Kennedy, 1960, Parker, 2004; Lang et. al, 2021). The upper plane bed is a flatbed condition at the transition between dunes and antidunes, that can be characterized by small amplitude and long wavelength bedforms that migrate downstream (Paola et al., 1989). Based on open channel flow experiments performed with coarse sand (geometric mean size equal to 1.11 mm and 0.95 mm), Hernandez Moreira et al. (2016, 2020) suggested that, within the upper regime, a plane bed can also occur in the presence of bedload transport in sheet flow mode (Hernandez Moreira et. al, 2020). The term antidune was coined by Gilbert & Murphy (1914), to describe bedforms that were moving upstream, but as knowledge advanced, researchers discovered that antidunes also move in the downstream direction (Kennedy, 1960; Hernandez Moreira et. al, 2020).

The Otaki River located in the North Island of New Zealand, was founded to be created by the formation of antidunes (Araya & Masuda, 2001). Madeno Creek at the Great Sand Dunes National Park and Preserve in Colorado, USA is another example of a stream where antidunes are found in nature. Madeno Creek experiences surge flows that produce antidunes up to a foot high in the spring season (Langford & Bracken, 1987).

Cyclic steps can be considered as very long upstream migrating antidunes characterized by the presence of a hydraulic jump on their lee faces (Covault et. al, 2017).

In this thesis, I summarize the results of laboratory experiments specifically designed to investigate the role of sediment supply and grain size on the formation of upper regime bedforms. Of the 17 experiments discussed herein, I performed seven of them, and Sadegh Jafarinik performed the other ten. The experiments by Ricardo Hernandez Moreira (2016, 2020) performed in the same experimental facility and with relatively coarse sand are also used in the analysis presented below.

CHAPTER 2

LABORATORY EXPERIMENTS

2.1 Experimental Overview

Laboratory experiments were conducted in the Hydraulics Laboratory at the Department of Civil and Environmental Engineering, University of South Carolina. The main objective was to observe and quantify how bedform type and geometry is affected by sediment supply rate and grain size. Sediment supply and flow discharge were chosen with the intended goal to obtain equilibrium bed configurations that evolve from lower regime to upper regime bedforms, with upstream bedforms migrating in the upstream and downstream directions. Sediment geometric mean grain sizes D_g ranged between 0.22 mm and 0.87 mm, flow rates Q_w varied between 5 l/s and 30 l/s, and sediment feed rates between 0.5 kg/min and 20 kg/min. Sediment sizes were chosen based off the range where sand waves occur and what material is locally available (Guy et al. 1966).

2.2 Experimental Setup

Experiments were conducted in a glass wall sediment feed flume. The flume is 13 m long, 0.5 m wide and 0.9 m deep. A custom sediment trap is placed 9 m downstream of the flume entrance and a tailgate controls the downstream water surface level. A calibrated orifice plate and a Dwyer series 490 wet-wet manometer were used to measure the flow rate from the head tank. To decrease the sediment supply needed for experiments and the occurrence of three-dimensional bedforms, the cross-section of the

test reach was narrowed to 0.19 m with the use marine plywood. A schematic view of the flume is depicted in Figure 2.1. In the first 2 m of the flume the cross section is gradually narrowed to 0.19 m to obtain a 7 m long experimental test reach (Jafarinik et. al, 2019; Hernandez et. al, 2020).

2.3 Experimental Procedure

All experiments started from a net-depositional or net-erosional (disequilibrium) condition and continued until the bed level averaged over a series of bedforms did not change in time (equilibrium). At equilibrium, suspended sediment concentration was measured at the downstream end of the test reach and the experiment terminated. Table 2.1 summarizes the experimental conditions of the laboratory experiments presented herein. The experiments are named by the run number and distinguished by the experimentalist, for example, 1-SS denotes the first experiment ran by Sydney Sanders and 9-SJ denotes the ninth experiment ran by Sadegh Jafarinik. In the proceeding columns, geometric mean diameter of the sediment D_g, flow rate Q_w, and mass feed rate G_s are presented. In this thesis I primarily report on the experiments I performed.

Experiment 1-SS started with a 10 cm thick flat layer of sediment with D_g equal to 0.43mm. The equilibrium bed of one experiment was used as initial condition for the next experimental run. For example, the initial deposit in experiments 2-SS and 5-SS, was the equilibrium bed of experiments 1-SS and 4-SS respectively. After experiment 3-SS, a ~3 cm layer of sediment mix with D_g equal to 0.34 mm was sprinkled over the existing deposit to perform experiments with a finer sediment grain size. This process was repeated once more before experiment 7-SS to use coarser sediment with D_g equal to

0.62 mm. The duration of an experiment varied between 45 minutes to two hours depending on the initial condition and the feed rate. As the sediment size decreased, the time it took to reach equilibrium conditions decreased.

2.3.1 Sediment Grain Size Distributions

The grain size distributions of the sediment used in the experiments are presented in Figure 2.2. Two uniform quartz sands with geometric mean diameters are equal to 0.22 mm and 0.62 mm were used to obtain the sediment mixtures used in the experiments. Experiments 1-3-SS were performed with non-uniform sand with D_g equal to 0.43 mm and geometric standard deviation σ_g equal to 1.85 mm. For experiments 4-6-SS the grain size distribution of experiments 1-3-SS was made finer by adding one scoop of fine sand for every one scoop of sediment mixture, resulting in a new mixture with D_g equal to 0.34 mm and σ_g equal to1.95 mm. In Figure 2.2, I also report the grain size distribution of the experiments performed by Sadegh Jafarinik with D_g equal to 0.87 mm and $\sigma_g$equal to 1.48 mm.

2.3.2 Bed and water surface profiles

On the glass wall and at the top of the flume there are vertical and horizontal rulers which indicate the distance from the flume entrance and the elevation above the flume bed. Bed and water surface elevations were measured at every 10 cm interval moving downstream with ruler readings (Hernandez Moreira et al., 2020). The first measurement was recorded 3.50 m from the flume entrance and the last measurement was taken at 8.90 m from the flume entrance. During the experiments, measured values were reported in a spreadsheet, plotted and the slopes of the best fit lines were computed to

estimate the bed slope and the water surface slope. When the bed and water surface slopes did not significantly change in time, the flow and the sediment transport were deemed to be at equilibrium (Viparelli et al., 2015, Hernandez Moreira et al., 2020). Equilibrium profiles were then used to compute flow parameters, as outlined in sections 2.3.3 and 2.3.4.

2.3.3 Removal of Sidewall Effects from laboratory data

Figure 2.1 depicts a schematic of the laboratory setup, where the sediment-covered bed is rough compared to the non-erodible glass walls of the flume itself and the water depth is of the same order of magnitude of the channel width. Because of this, the difference in roughness between the bed and the side walls, glass and marine plywood, must be accounted for to properly estimate the bed shear stress acting on the rough bed.

Here we follow the procedure introduced by Vanoni & Brooks (1957) as implemented by Chiew & Parker (1994). The cross section is divided into two component regions, the bed, and the wall region, ensuing a unique shear stress for the bed and the wall. It is assumed that the Darcy-Weisbach resistance relationship holds for the entire cross section and for both the bed and wall regions. Furthermore, the mean flow velocity, U, and the energy gradient S_f are assumed to be the same for the cross section, the bed, and the wall regions.

For the following equations below the subscripts cs, b and w, signify the entire cross-section, the bed, and the wall regions respectively. Given the previous assumptions, the mass and momentum conservation equations reduce to the following forms:

$$A_{cs} = A_b + A_w \qquad (2\text{-}1)$$

$$C_{f_{cs}} P_{cs} = C_{f_w} P_w + C_{f_b} P_b \qquad (2\text{-}2)$$

where A denotes the cross-sectional area, P the wetted perimeter, C_f a non-dimensional friction coefficient equal to the Darcy-Weisbach friction coefficient f divided by 8. For the rectangular cross section considered herein, P of the bed region is equal to the width of the cross section and the P of the wall region is equal to $2H$, where H is the water depth.

For the assumption of equal energy gradient for the entire cross-section and both the bed and wall regions, the Darcy-Weisbach relation is rewritten as:

$$\frac{C_{f_{cs}} U^2}{gr} = \frac{C_{f_b} U^2}{gr_b} = \frac{C_{f_w} U^2}{gr_w} \qquad (2\text{-}3)$$

where g is the acceleration of gravity and r the hydraulic radius equal to the cross-sectional area divided by the wetted perimeter, $r = A/P$. Using the definition of Reynolds number, $Re = rU/\nu$, where ν denotes the kinematic viscosity of water, equation (3) is rewritten as:

$$\frac{C_{f_{cs}} U^2}{Re_{cs}} = \frac{C_{f_b} U^2}{Re_w} = \frac{C_{f_b} \mathrm{U}^2}{Re_w} \qquad (2\text{-}4)$$

To solve equations 2-1,2-2 and 2-4, in the unknowns A_b, A_w, C_{f_b}, C_{f_w}, the Nikuradse equation for smooth pipes is used:

$$\frac{1}{\sqrt{f_w}} = 0.86 \ln\left(4Re_w\sqrt{f_w}\right) - 0.8 \qquad (2\text{-}5)$$

An iterative method is necessary to solve Equations 2-1, 2-2, 2-4, and 2-5. The first estimate of f_w is obtained from the Blasius equation in the following form:

$$f_w=0.301\ (\frac{f}{Re})^{\frac{1}{5}} \quad (2\text{-}6)$$

2.3.4 Flow Resistances: Skin Friction and Form Drag

In presence of bedforms, the flow resistance may be affected by the interaction between the flow and the bedform (form drag). Stresses that act tangentially to the bed, known as skin friction, are critical to sediment entrainment and bedload transport. When no bedforms are present, the drag on the bed is only associated with skin friction (Parker, 2004).

For the computation of skin friction flow resistance and bed shear stresses, an ideal flatbed configuration is considered. This ideal flow has the same grain roughness, energy slope S_f, and mean flow velocity U as there is presence of bedforms. Using this ideal flow, the hydraulic radius and the bed friction coefficient associated with skin friction, r_{bs} and $C_{f_{bs}}$ respectively, are computed with the use of the 1) Manning-Strickler relation, equation (2-7), 2) the product of the hydraulic radius and the energy slope to compute the bed shear stress associated with skin friction, equation (2-8), 3) the definition of hydraulic radius and shear velocity, equations (2-9) and (2-10). The equations used on the calculations take the form:

$$C_{f_{bs}}{}^{-0.5} = \frac{U}{u^*_s} = \alpha_r(\frac{r_{bs}}{k_s})^{1/6} \quad (2\text{-}7)$$

$$\tau_{bs} = \rho g r_{bs} S_f \quad (2\text{-}8)$$

$$r_{bs} = \frac{A_{bs}}{B} \quad (2\text{-}9)$$

$$u^*_s = \sqrt{\frac{\tau_{bs}}{\rho}} \quad (2\text{-}10)$$

where α_r is a constant equal to 8.1 (Parker, 1991). The roughness height $k_s = n_k D_{sg90}$ with D_{s90} denoting the diameter of the bed surface sediment such that 90% of the bed surface sediment is finer, and n_k being a constant with the value of 2 (Parker, 2004). Furthermore, A_{bs} denotes the area of the bed region in the ideal flatbed configuration, B is representative of the rectangular channel cross-section width of the flume, and u^*_s is the shear velocity associated with skin friction.

The values of hydraulic radius r_{bs} and shear velocity u^*_s are iteratively calculated using equations 2-7 & 2-8. The Shields number associated with skin friction $\tau^*_{sg} = u^*_s{}^2/RgD_{sg}$ where R is the submerged specific gravity of the sediment and D_{sg} is the geometric diameter of the sediment on the bed surface.

Due to the relatively high bed shear stresses, in the experiments presented in this thesis the bed surface is assumed to be unarmored, that is the geometric mean size D_g and the D_{90} of the bed surface sediment are assumed to the equal to those of the sediment feed (Parker & Klingeman, 1982).

2.3.5 Suspended Sediment Concentration

The volumetric suspended sediment concentration, c, was measured by a rack of six siphons located approximately 2 cm apart. The apparatus was placed at the downstream end of the sediment deposit, just before the sediment trap; a schematic view can be seen in Figure 2.1. The samples were collected into 1500 cm^3 containers, the

suspension was then filtered, the sediment was dried in the oven weighted and the volumetric concentration was computed. To convert sediment weight into volumes, a density equal to 2.65 gr/cm^3 was used.

Measurements of suspended sediment concentration were performed in the experimental runs 1-SS – 6B-SS, 5-SJ – 7SJ, 9-SJ and 10-SJ. In the SS experiments, the rack of siphons was positioned on the flume sidewalls, so that the distance between the siphon closest to the deposit and the deposit z_b varied from one experiment to the other. In the SJ experiments, the elevation of the rack of siphons varied from one experiment to the other to maintain z_b equal to few percent of the flow depth. For this reason, the suspended sediment concentration measured at the siphon closest to the deposit in the SJ experiments is considered equal to its near bed value.

The Rouse profile represents the vertical variation of sediment in suspension in the water column in the case of equilibrium suspension. Equilibrium suspension refers to a condition in which sediment deposition from suspension is equal to the entrainment of sediment in suspension for the channel bed. The mathematical form of the Rouse profile is:

$$\frac{c}{c_b} = \left[\frac{(1-\zeta)\zeta_b}{(1-\zeta_b)\zeta}\right]^{\frac{v_s}{\kappa u^*}} \quad (2\text{-}11)$$

where c is the volumetric suspended sediment concentration averaged over turbulence at elevation z above the bed (in this case the height of the siphon above the bed), v_s is the particle settling velocity, either a known or measured parameter. In this study, v_s is the settling velocity of the geometric mean size of the suspended sediment computed with the Dietrich (1982) relation. Due to the small amount of sediment collected with the siphons,

the grain size distribution of the suspended sediment is assumed to be similar to that of the sediment that deposited downstream of the sediment trap. Additionally, κ is the von Karman constant with a value of 0.41 and u^* is the shear velocity obtained from the water surface and bed equilibrium profiles. The non-dimensional elevation above the channel bed, ζ is equal to z/H, with H being the flow depth; accordingly, $\zeta = 0$ on the channel bed and $\zeta = 1$ at the free surface. The non-dimensional near bed reference elevation, ζ_b, is where the suspended sediment concentration is equal to an unknown near-bed value of c_b.

The Rouse profile is fitted to the SS experimental data using two different approaches. In the first approach, the near bed suspended sediment concentration c_{b1} is set equal to the suspended sediment concentration measured at the siphon closest to the bed. Equation 2-11 is solved directly, with z_b equal to the non-dimensional elevation of the siphon closest to the bed. The Rouse profile is compared to the data to determine how far the suspended sediment is far from equilibrium. In the second approach, equilibrium suspension is assumed and the near bed suspended sediment concentration c_{b2} is estimated to fit the data with the Rouse profile. In these calculations z_b is equal to a value at 5% of the experimental flow depth and the entrainment rate of sediment in suspension E is assumed to be equal to c_b (e.g., Garcia & Parker, 1991; Wright & Parker, 2004).

2.4 Table

Table 2.1 Summary of Experimental Conditions. Experiments were run in two different experimental sets and are denoted by the experimentalist's initials (i.e. SS and SJ) along with each unique run number where experiment 1 ran by Sydney Sanders is denotated as 1-SS and experiment 3 ran by Sadegh Jafarinik is denoted 3-SJ. Here D_g = geometric mean diameter, Q_w= flow discharge, and G_s= mass sediment feed rate.

Run name	$\boldsymbol{D_g}$ **(mm)**	$\boldsymbol{Q_w}$ **(kg/min)**	$\boldsymbol{G_s}$ **(kg/min)**
1-SS	0.43	30	10
2-SS	0.43	20	10
3-SS	0.43	10	10
4-SS	0.34	10	10
5-SS	0.34	10	15
6A-SS	0.34	10	20
6B-SS	0.34	5	20
7-SS	0.62	10	10
1-SJ	0.87	15	1.5
2-SJ	0.87	15	6
3-SJ	0.87	15	16
4-SJ	0.87	8	6
5-SJ	0.62	15	1
6-SJ	0.62	15	2.2
7-SJ	0.62	15	6.9
8-SJ	0.22	15	0.6
9-SJ	0.22	8	0.6
10-SJ	0.22	8	2.2

2.5 Figure Captions

Figure 2.1. Schematic view of the experimental setup (not to scale). Depicted is a sediment feed flume at which water inflows at a constant flow rate from a head tank and discharges into the sump of the laboratory. The sediment feeder ejects the sediment mix into the flume and the excess sediment is collected into the sediment trap. Sediment that travels past the sediment trap is collected as representative of the sediment transported in

suspension; a six-siphon rake is placed in during experimental runs to collect suspended sediment in the water column.

Figure 2.2. Grain Size Distributions of the sediment used in the experiments presented in this study.

2.6 Figures

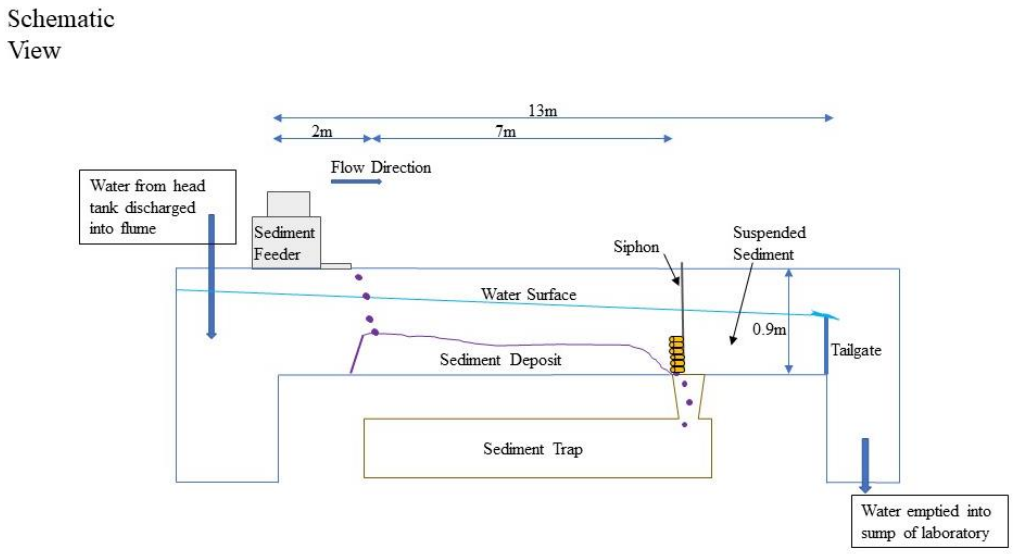

Figure 2.1. Schematic view of the experimental setup (not to scale). Depicted is a sediment feed flume at which water inflows at a constant flow rate from a head tank and discharges into the sump of the laboratory. The sediment feeder ejects the sediment mix into the flume and the excess sediment is collected into the sediment trap. Sediment that travels past the sediment trap is collected as representative of the sediment transported in suspension; a six-siphon rake is placed in during experimental runs to collect suspended sediment in the water column.

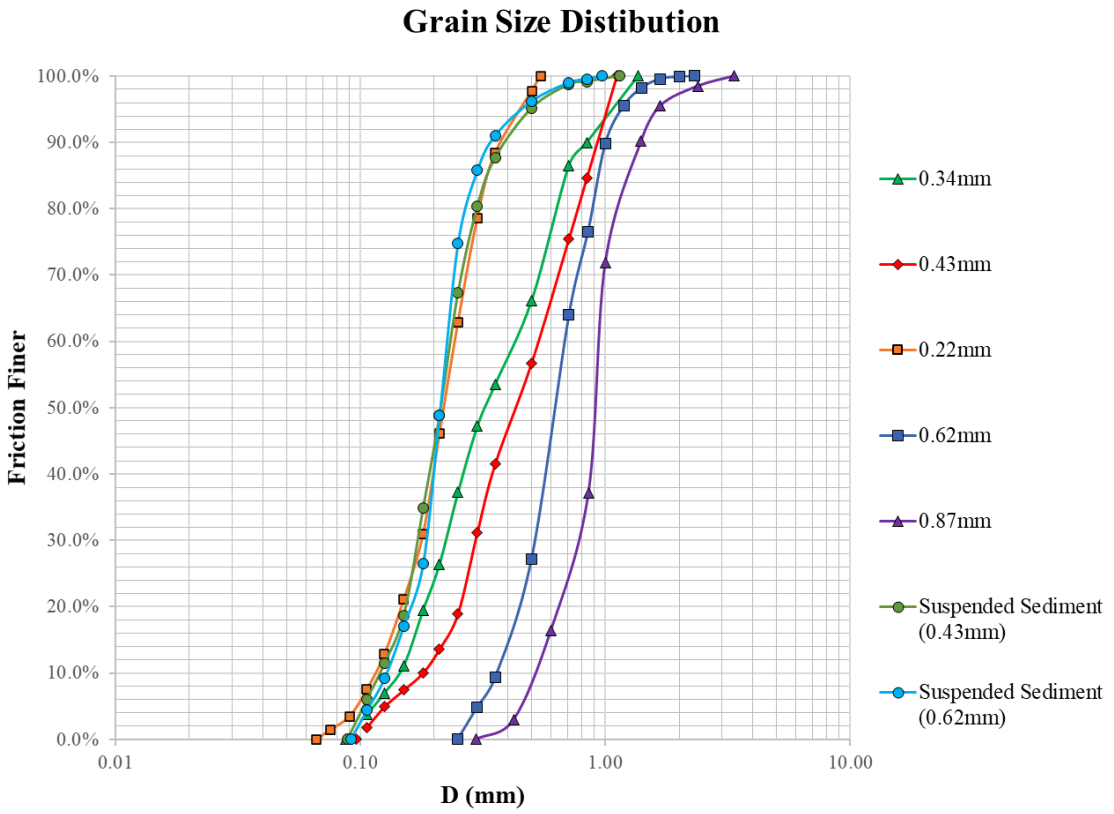

Figure 2.2. Grain Size Distributions of the sediment used in the experiments presented in this study.

CHAPTER 3

RESULTS

3.1 Overview

Table 3.1 presents the experimental results in terms equilibrium bed slope S, equilibrium flow depth H; Froude number associated with skin friction Fr_o, equilibrium bedform height and wavelength Δ and λ, bedform migration rate v and bed configuration. Bedform heights and wavelengths were measured using rulers attached to the flume and the bedform migration rate was estimated by capturing the time it took for the crest of the bedform to move a minute (in either direction) or wash away, referencing the ruler readings from the flume. The resulting equilibrium bed configuration was classified using observations during the experiments of the bed and water surface and the Engelund (1970) stability diagram. Bed configurations are abbreviated as follows: D as dunes, WD as washed-out dunes, UP as upper plane bed, SW as standing waves, UA as upstream migrating antidunes, DA as downstream migrating antidunes, and PS as plane bed with bedload transport in sheet flow mode. The term *none* in Table 3.1 indicates that the bedform height or migration rate could not be measured.

3.2 Bed Configurations using the Engelund Stability Diagram (1970)

The Engelund (1970) stability diagram is utilized to classify the bed configurations in terms of the non-dimensional wavenumber *k* and the Froude number associated with skin friction Fr_o. These parameters are defined as follows:

$$k = \frac{2\pi H_o}{\lambda} \quad (3\text{-}1)$$

$$Fr_o = \frac{U}{\sqrt{gH_o}} \quad (3\text{-}2)$$

where H_o is the flow depth associated with skin friction (no form drag) computed with equations (2-7) -(2-10) and the flow velocity is denoted as U. The Froude number associated with skin friction is represented on the vertical axis and the non-dimensional wave number is on the horizontal axis. The black lines in Figure 3.1 identify three regions of the *k*, Fr_o plane corresponding to the lower regime, and the upper regime with bedform migrating upstream and downstream. Symbols in Figure 3.1 represent the experimental data of Table 3.1 and of the experiments performed in the same flume by Hernandez Moreira (2016) using sediment with geometric mean size equal to 0.95 mm and 1.11 mm. Colors indicate the sediment geometric mean size and the symbol represents the bed configuration.

In the Engelund (1970) analysis, subcritical conditions occur when $Fr_o <= [\tanh(k)/k]^{1/2}$, and the response of the flow to the presence of bedforms results in the water surface and the water depth to be out of phase with the bed. In other words, low water elevation corresponds to the crest and high water elevation corresponds to the trough. In addition, the flow on the trough is deeper than on the crest. Thus, the flow

accelerates from the trough to the crest and decelerates from the crest to the trough with a consequent downstream migration of the bedforms. Bed configurations in this region of the k, Fr_o plane correspond to the lower regime (dunes and washed out dunes of Table 3.1).

When Fr_o>=[tanh(k)/k]$^{1/2}$, supercritical conditions occur and the water surface is in phase with the bed, that is low water elevation corresponds to the trough and high water elevation corresponds to the crests. The bed configurations in this part of the k, Fr_o plane are those of the upper regime (antidunes and plane bed with sheet flow of Table 3.1). The supercritical flow response zone is separated into two areas indicating the direction of bedform migration. When Fr_o> [k tanh(k)]$^{-1/2}$ the water depth is out of phase with the bed, that is the flow is deeper on the trough than on the crest. As in the subcritical response case, the flow accelerates from the trough to the crest and decelerates from the crest to the trough so that the bedforms migrate downstream. On the contrary, when Fr_o< [k tanh(k)]$^{-1/2}$ the flow depth is in phase with the bed. In other words, the water depth is deeper on the crest than on the trough so that the flow decelerates from the trough to the crest and accelerates from the crest to the trough. As a consequence, the bedforms migrate in the upstream direction (Parker, 2004).

In Figure 3.1 the majority of the data pertaining to experiments with sediment finer than 0.62 mm are in the region with upstream migrating bedforms, while data from upper regime experiments with sediment coarser than 0.62 mm are in the region with downstream migrating bedforms. This suggests that sediment size may play a significant role on the migration direction of upper regime bedforms.

3.3 Upper regime bedforms

In the experimental runs of Table 3.1 different types of bed configuration were obtained by changing the discharge, the sediment feed rate, and the sediment size distribution. As general trends from Table 3.1 are observed, it is seen that bedform geometry and bed configuration change flow discharge decreases, the water depth, the sediment feed rate and grain size.

The increase in feed rate causes the bedform wavelength to increase, as shown in Figure 3.1 for the experimental runs 4-SS - 6A-SS performed with sediment with geometric mean size equal to 0.34 mm. In Figure 3.1 pictures taken during the experiments clearly show that when the feed rate G_s increases from 10 kg/min to 15 kg/min to 20 kg/min and the flow rate Q_w equals 10 l/s, the bedform wavelength increases from 50 cm to 80 cm. Similar behavior is observed in experimental runs performed with coarser sand in experimental runs 2-SJ and 3-SJ (D_g = 0.87 mm), and 6-SJ – 7-SJ (D_g = 0.62 mm). Runs 2-SJ and 3-SJ were performed with sediment with D_g= 0.87 mm and flow discharge Q_w=15 l/s. In these runs, the wavelength increases from 30 cm to 45 cm as the feed rate increases from 6 kg/min to 16 kg/min (Figure 3.2a). The sediment used in runs 6-SJ – 7-SJ had D_g = 0.62 mm, the flow discharge was 15 l/s and, as the feed rate increased from 2.2 kg/min to 6.9 kg/min, the wavelength increased from 25 cm to 35 cm, as shown in Figure 3.2b.

The change in equilibrium bedform height due to an increase in sediment feed rate varied depending on the sediment grain size. In the runs 4-SS – 6-SS performed with relatively fine sand, the equilibrium height of the upstream migrating antidunes increased

with the sediment transport rate. Conversely, in the runs 2-SJ and 3-SJ, and 6-SJ and 7-SJ performed with relatively coarse sand, the equilibrium height of the downstream migrating antidunes decreased in response to an increase in sediment transport rate. In particular, the experimental runs with D_g = 0.87 mm (2-SJ and 3-SJ) antidunes evolved into an upper plane bed with bedload transport in sheet flow mode, and in experimental runs with D_g = 0.62 mm (6-SJ and 7-SJ) the downstream migrating antidunes evolved into upper regime plane bed. The sediment used in the experimental runs 1-SS - 3-SS had a geometric mean diameter of 0.43 mm. As the flow discharge decreased from 30 l/s to 20 l/s to 10 l/s, respectively, the water depth also decreases and the bed configuration changed from upper plane bed, to standing waves to upstream migrating antidunes (Figure 3.3a). Another change in bed configuration associated with a change in flow discharge, and thus water depth, is observed in experimental runs 2-SJ and 4-SJ (Figure 3.3b). As the flow discharge decreased from 15 l/s to 8 l/s, the water depth also decreased, and the bed configuration changed from downstream migrating antidunes to upper plane bed. A change in bedform shape associated with a reduction in water depth is also observed in experimental runs 6A-SS and 6B-SS, as the discharge was decreased from 10 l/s to 5 l/s the upstream migrating antidune height decreased and the wavelength increased (Figure 3.3c).

A change in antidune migration direction is observed between experimental run 6-SJ and 10-SJ. In these runs the feed rate is equal to 2.2 kg/min, water discharge decreases from 15 l/s (6-SJ) to 8 l/s (10-SJ), the sediment geometric mean size decreases from 0.62 mm (6-SJ) to 0.22 mm (10-SJ). The antidunes migrate in the downstream direction in run 6-SJ and in the upstream migration in run 10-SJ. The effect of sediment

size on upstream migrating antidunes is also observed by comparing experimental runs 3-SS, 4-SS and 7-SS performed with flow discharge of 10 l/s, feed rate of 10 kg/min and with sediments with geometric mean sizes of 0.43 mm, 0.34 mm and 0.62 mm, respectively. The antidune wavelength did not change with sediment size, however antidune height and migration rates were highest in the runs with the finest sediment and were smallest in the runs with the coarsest sediment.

3.4 Non-Dimensional Plots

The description of the laboratory data presented above suggests that 1) sediment size, and thus the mode of bed material transport, plays a role on the migration direction and the type of upper regime bedforms (Figure 3.1), 2) the wavelength of upper regime bedforms tends to increase with the sediment supply (Table 3.1 and Figure 3.2), and 3) changes in water depth/flow discharge result in a change of bedform geometry or bed configuration (Table 3.1 and Figure 3.3).

To investigate if these observations can be generalized, the data of Table 3.1 and those by Hernandez Moreira et al. (2016) are presented in non-dimensional forms. The sediment geometric mean size is used to make the wavelength and the flow depth non-dimensional. The water discharge is used to make the volumetric sediment feed rate non-dimensional. The ratio between the sidewall- corrected shear velocity u_* and the fall velocity of the geometric mean size of the sediment, v_{sg}, is used to determine if significant suspended bed material load ($u_*/v_{sg} > 1$) can be expected.

The non-dimensional wavelength, flow depth and the ratio u_*/v_{sg} are plotted against the ratio between the volumetric sediment transport rate Q_s and the flow discharge

Q_w in Figure 3.4, panels a, b and c respectively. The color scheme and the symbols used in Figure 3.4 to indicate the sediment grain size and the bed configuration are those used in Figure 3.1.

In the panels of Figure 3.4 the experimental points clearly indicate that, for values of Q_s/Q_w smaller than 0.0003 the bed configuration is in the lower regime. As Q_s/Q_w increases, the bed configuration transitions to the upper regime for values of $Q_s/Q_w >$ 0.0007. In the upper regime, values of $Q_s/Q_w < 0.00175$ correspond to downstream migrating antidunes. For values of $Q_s/Q_w > 0.0032$, in case of relatively coarse sand (D_g ≥ 0.62 mm) the bed tends to become plane with bedload transport in sheet flow mode. In the case of relatively fine sand ($D_g < 0.62$), upstream migrating antidunes form.

As the bed configuration transitions from lower to upper regime, the non-dimensional bedform wavelength (Figure 3.4a) and the non-dimensional water depth decrease (Figure 3.4b). A decrease of the dimensional water depth from lower to upper regime was also observed in the Vanoni (1974) non-dimensional bedform plots. For increasing values of Q_s/Q_w the downstream migrating antidunes become longer (λ/D_g increases) and the non-dimensional flow depth (H/D_g) increases. In the case of $D_g \geq 0.62$ mm, the bedform height decreases, the bedload transport capacity of the flow increases, and the bed configuration transitions to upper plane bed with bedload transport in sheet flow mode (Hernandez Moreira et al., 2020). In the case of fine sand, on the other hand, a change in antidune migration direction is observed and the bedform length continues to increase suggesting a tendency to transition toward cyclic steps.

Figure 3.6c confirms that in the experiments with downstream migrating bedforms the bed material was preferentially transported as bedload transport, while upstream migrating bedforms occurred in presence of significant suspended bed material load only. These results are in agreement with the analysis presented by Engelund (1970), antidunes tend to migrate upstream in the absence of bedload transport but they can migrate downstream in the case of coarse sand preferentially transported as bedload (see Fig. 11 in Engelund, 1970).

3.5 Suspended Sediment Concentration

The first step in the analysis of the measurements of suspended sediment concentration was to fit the Rouse profile to the data to determine how far the experiments were from equilibrium suspension. The comparison between the data collected in the experimental runs 2-SS and 6-SJ are respectively presented in panels a and b of Figure 3.5, where the dots are the experimental points and the lines represent the Rouse profile, equation (2-11). The Rouse profile of Figure 3.5 a was computed assuming that the near bed concentration was equal to the value measured at the siphon closest to the deposit, c_{b1}.

Measured and computed suspended sediment concentration profiles of Figure 3.5 have a different shape due to the differences between the experimental conditions and the sediment grain size distribution. Experiment 6-SJ was performed with uniform sediment with D_g = 0.62 mm and experiment 2-SS was performed with non-uniform sediment with D_g = 0.43 mm, which was a mixture of two uniform sediments with D_g =0.22 mm and D_g = 0.62 (Figure 2-2). It is thus reasonable to expect that the sediment in suspension in experiment 2-SS was finer than the sediment suspended in experiment 6-SJ. In addition,

the sediment feed rate was equal to 10 kg/min in experiment 2-SS and to 2.2 kg/min in experiment 6-SJ. Thus, the entrainment rate of sediment is suspension in experiment 2-SS is expected to be larger than in experiment 6-SJ and this will also favor a higher suspended sediment concentration in the upper part of the water column.

In the case of equilibrium suspension, the near bed concentration of suspended sediment c_b is equal to the non-dimensional rate of entrainment of sediment in suspension E, which can be predicted with empirical relations when the properties of the suspended sediment and of the fluid and the shear velocity associated with skin friction are known (Parker, 2004).

To further investigate if our experiments can be compared with other experimental datasets, I compared the measurements of near bed volumetric suspended sediment concentrations with entrainment rates predicted with the relations by Garcia & Parker (1991) and Wright & Parker (2004). These entrainment relations take the form

$$E = \frac{AZ_u^5}{1+\frac{A}{0.3}Z_u^5} \qquad (3.1)$$

where A is a constant equal to $1.3 \cdot 10^{-7}$ and to $7.8 \cdot 10^{-7}$ for the Garcia & Parker (1991) and Wright & Parker (2004) relations, respectively, and Z_u is a non-dimensional number defined as follows for the case of uniform sediment

$$Z_{u,GP} = \frac{u_s^*}{v_s} Re_p^{0.6} \qquad Z_{u.WP} = \frac{u_s^*}{v_s} Re_p^{0.6} S^{0.07} \quad (3.2a, b)$$

where the subscripts GP and WP respectively denote Garcia & Parker and Wright & Parker, u^*_s is the shear velocity associated with skin friction, v_s is the settling velocity of the sediment, S is the be slope and Re_p is the particle Reynolds number defined as

$\sqrt{RgD}D/\nu$, with R being the submerged specific gravity of the sediment, D the sediment grain size, g the acceleration of gravity and ν the kinematic viscosity of the fluid.

In the SS experiments, the grain size of the suspended sediment was measured (D = 0.21 mm), so the entrainment rate E can be estimated from the data and then compared against the experimental measurements. In the SJ experiments, the grain size of the suspended sediment was not measured, and it is assumed to guarantee a reasonable agreement between equations (3-1) and (3-2) and the measured near bed concentrations c_b. The grain size of the suspended sediment in the SJ experiments is assumed to vary between 0.12 mm and 0.31 mm, which is reasonable given the grain size distributions of Figure 2.2, where the finest diameters of the grain size distributions are linearly interpolated on a log2 scale from the data (Parker, 2004).

As outlined in Chapter 2, the near bed volumetric suspended sediment concentration in the SS experiments was also estimated to have a reasonably good fit of the experimental data with the Rouse profile c_{b2}, under the assumption that z_b = 0.05. Due to the paucity of the experimental points, meaningful statistical analysis could not be performed, and the goodness of the fit was judged by eyes.

The comparison between measured entrainment rates and those predicted with equations (3-1) and (3-2) is presented in Figure 3.6, where the continuous lines in panels a and c respectively represent the entrainment relation by Garcia & Parker (1991) and Wright & Parker (2004) and the dots represent the experimental points. The differences between measured and predicted entrainment rates are also presented in panels b and d, where the 1:1 line represents the perfect agreement between model and data. The

comparison between model and data, as well as the scatter of the data, in Figure 3.6 is comparable with that reported in other studies such as Garcia & Parker, (1991), Wright & Parker (2004) and Moodie et al. (2000).

3.6 Table

Table 3.1 Summary of Experimental Results, where S= slope, H= flow depth, Δ = bedform height, λ= bedform wavelength, v = migration rate indicating how fast bedforms are moving in their perspective direction. The bed configuration is reported using he following abbreviations: D as dunes, WD as washed-out dunes, UP as upper plane bed, SW as standing waves, UA as upstream migrating antidunes DA as downstream migrating antidunes, and PS as plane bed with bedload transport in sheet flow mode. The term *none* in the bedform height columns means that bedform height and migration could not be measured.

Run Name	$\boldsymbol{S}$ **(-)**	**H (cm)**	$\boldsymbol{Fr_o}$ **(-)**	**Δ (cm)**	**λ (cm)**	**v (cm/min)**	**Bed Configuration**
1-SS	0.0072	13.14	1.06	none	0	none	UP
2-SS	0.0080	12.91	0.91	1.0	65	none	SW
3-SS	0.0150	3.96	2.13	2.0	50	35	UA
4-SS	0.0140	4.09	2.03	3.0	50	130	UA
5-SS	0.0130	4.98	1.18	4.5	80	150	UA
6A-SS	0.0150	5.52	1.32	5.5	90	none	UA
6B-SS	0.0180	3.89	1.44	3.0	100	none	UA
7-SS	0.0110	5.92	1.07	1.0	55	18	UA
1-SJ	0.0057	8.70	0.98	1.8	33	35	WD
2-SJ	0.0110	6.16	1.65	1.5	30	60	DA
3-SJ	0.0211	5.32	2.05	0.5	45	18	PS
4-SJ	0.0178	3.97	1.43	None	65	none	UP
5-SJ	0.0049	10.27	0.76	2.8	38	30	D
6-SJ	0.0074	7.91	0.90	3.2	25	29	DA
7-SJ	0.0135	4.87	2.35	None	35	none	UP
8-SJ	0.0024	10.17	0.85	0.8	10	17	WD
9-SJ	0.0029	8.42	0.83	1.0	10	18	WD
10-SJ	0.0049	6.36	1.08	1.8	28	17	UA

3.7 Figure Captions

Figure 3.1 Photos of bed deposits at 10 l/s and .34 mm experiments. Experimental photos of runs 4-6A-SS are displayed as the geometric mean diameter was .34mm and a constant flow discharge of 10 l/s. Here the evolution of upper regime bedforms was captured as the feed rate was manipulated between runs at 10, 15, and 20 kg/min resulting in upstream migrating antidunes with increased wavelengths.

Figure 3.2a Photos of bed deposits at 15 l/s and 0.87 mm experiments. Experimental photos of runs 2-3-SJ are displayed as the geometric mean diameter was .87 mm and a constant flow discharge of 15 l/s. Here the evolution of upper regime bedforms was captured as the feed rate was manipulated increased from 6 kg/min to 16 kg/min evolving downstream migrating antidunes to upper plane bed with sheet flow.

Figure 3.2b Photos of bed deposits at 15 l/s and 0.62 mm experiments. Experimental photos of runs 6-7-SJ are displayed as the geometric mean diameter was .62mm and a constant flow discharge of 15 l/s. Here the evolution of upper regime bedforms was captured as the feed rate was manipulated increased from 2.2 kg/min to 6.9 kg/min evolving downstream migrating antidunes to upper plane bed.

Figure 3.3 Engelund (1970) Stability Diagram. Phase Diagram (Engelund, 1970) used to classify bedform configurations in various experiments.

Figure 3.4 Non-dimensional plots a) non-dimensional wavelength (λ/D) versus the ratio between the volumetric sediment load and the flow discharge Q_s/Q_w, b) non-dimensional water depth (H/D) versus Q_s/Q_w, c) ratio between hear velocity and settling velocity u^*/v_{sg} versus Q_s/Q_w,

Figure 3.5 Comparison between the Rouse profile (continuous line) and the measured suspended sediment concentration profiles (dots). The near bed concentration is assumed equal to the deepest concentration measurement. a) experiment 2-SS and b) Experiment 6-SJ.

Figure 3.6 Comparison between the experimental data and the entrainment relations due to Garcia & Parker (1991) in panels a and b and Wright & Parker (2004) in panels c and d. The dots in a and c represent the experimental data and the continuous lines are the empirical entrainment relations. The continuous line in panels b and d represent the 1:1 line (or equality between measured and predicted values) and the dashed lines represent one order of magnitude from the 1:1 line.

3.8 Figures

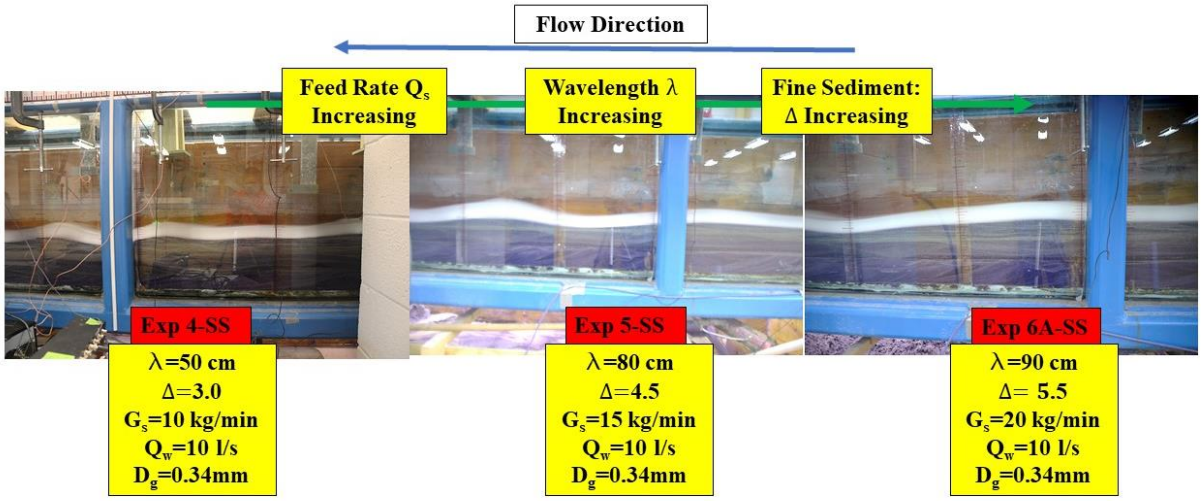

Figure 3.1 Photos of bed deposits at 10 l/s and .34 mm experiments.

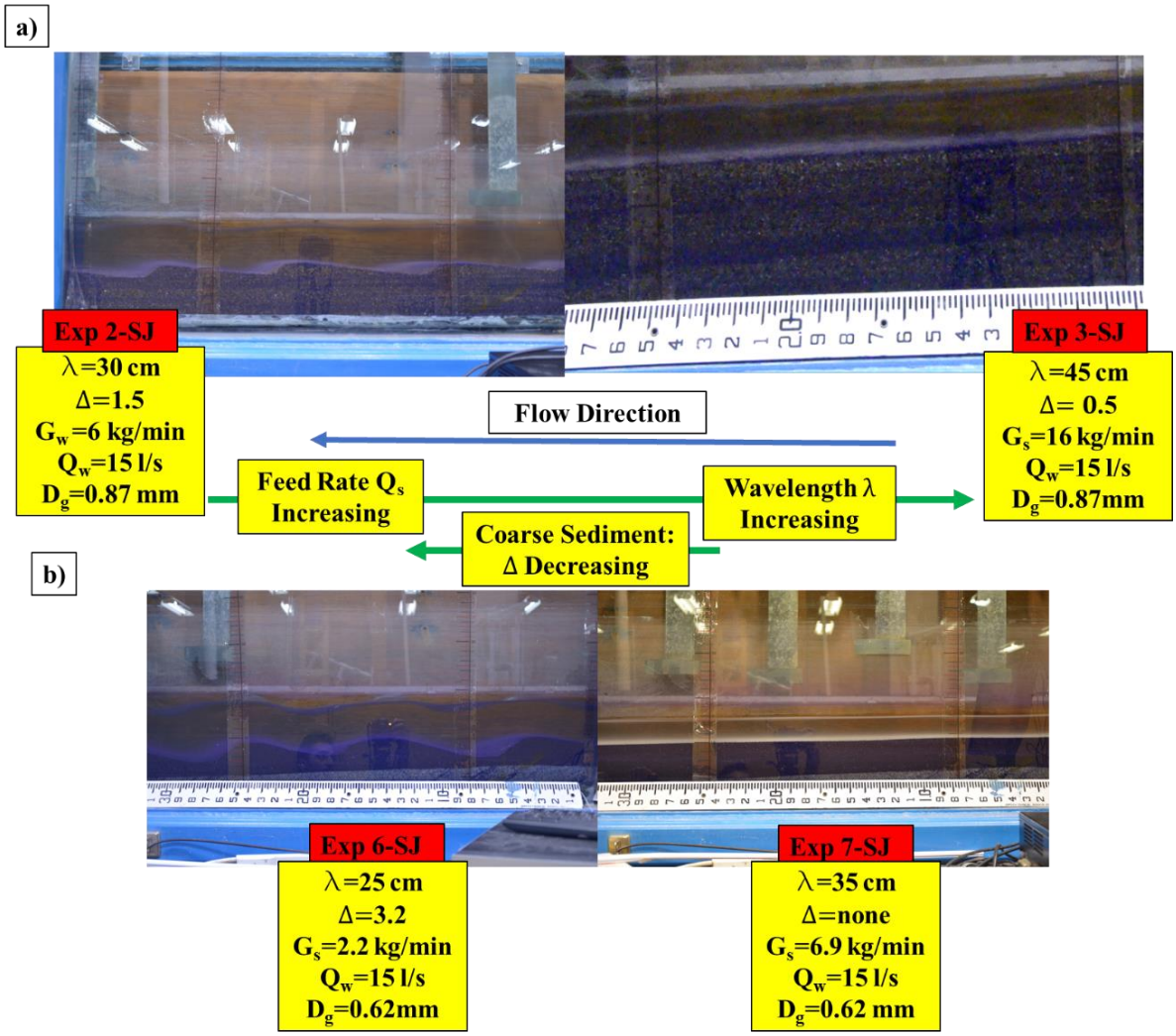

Figure 3.2 Photos of bed deposits a) at 15 l/s and 0.87 mm experiments and b) at 15 l/s and 0.62 mm experiments.

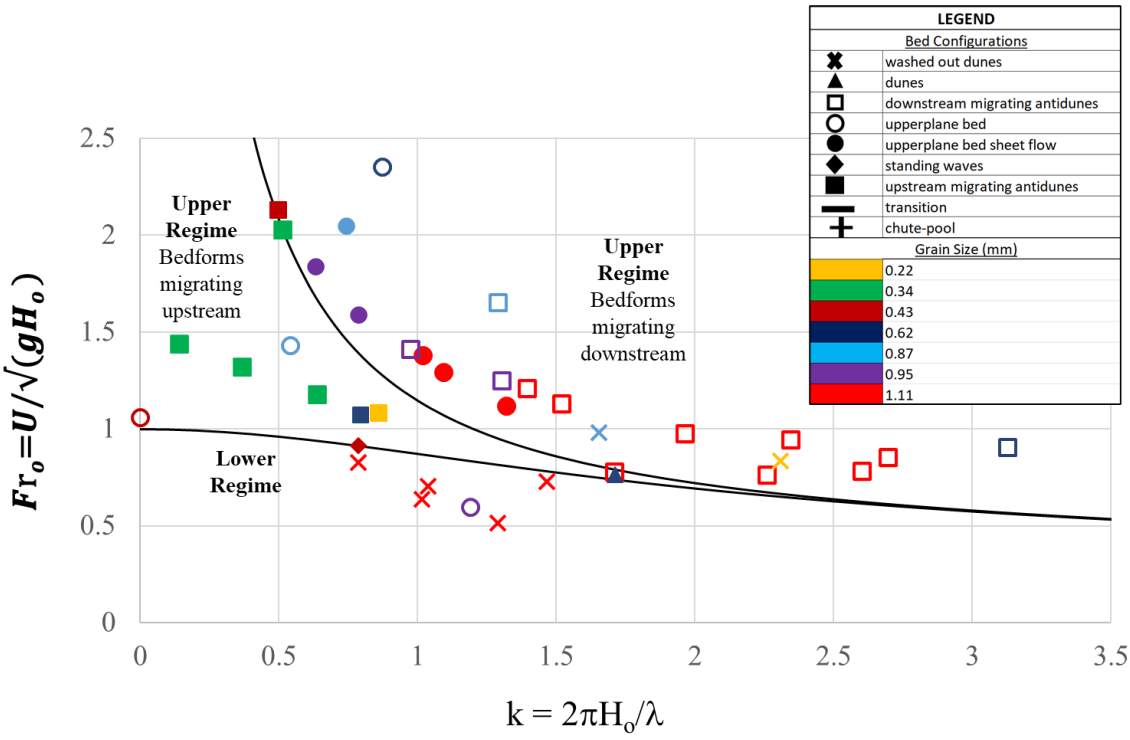

Figure 3.3 Engelund (1970) Stability Diagram

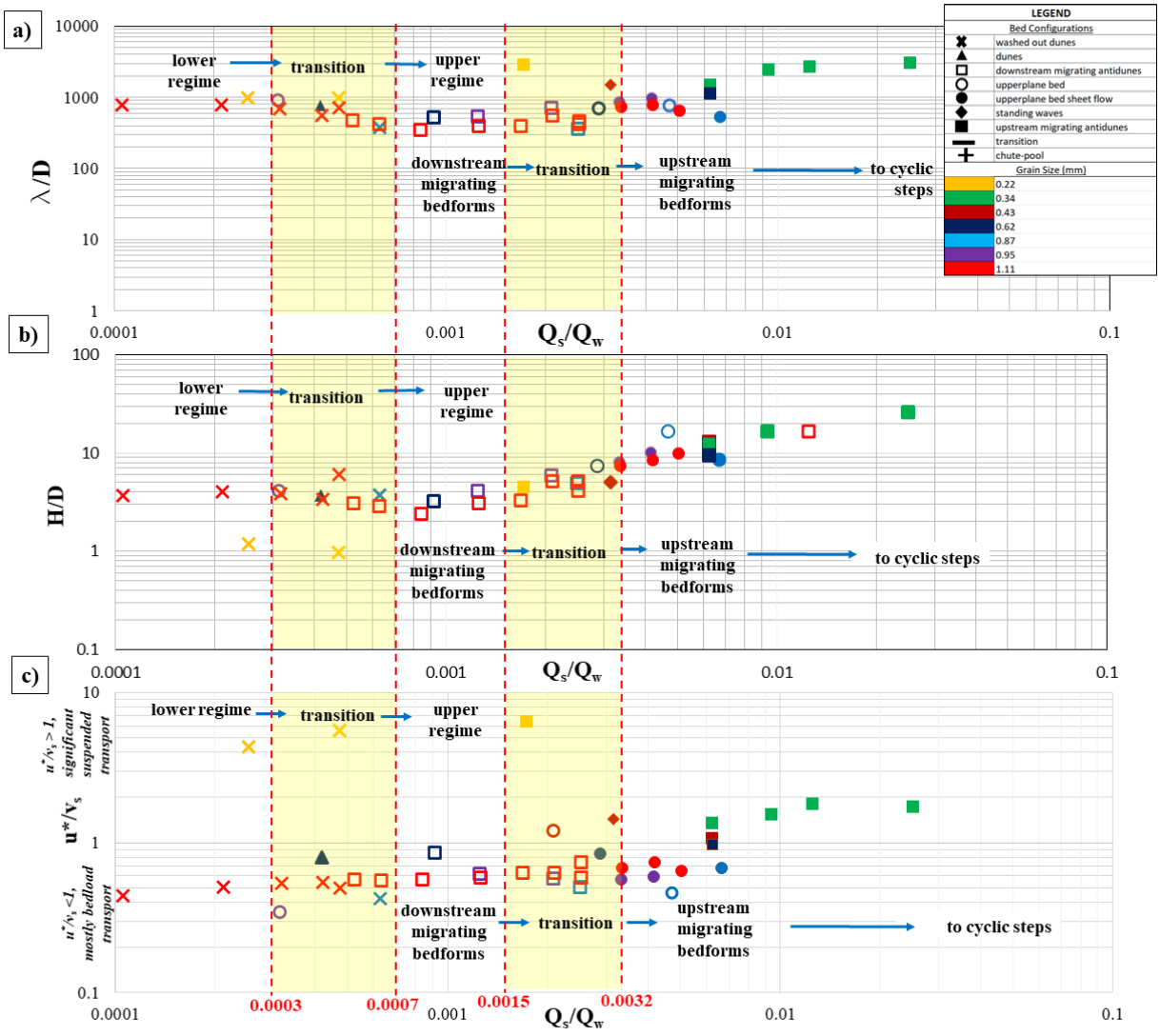

Figure 3.4 Non-dimensional plots a) non-dimensional wavelength (λ/D) versus the ratio between the volumetric sediment load and the flow discharge Q_s/Q_w, b) non-dimensional water depth (H/D) versus Q_s/Q_w, c) ratio between shear velocity and settling velocity u^*/v_{sg} versus Q_s/Q_w,

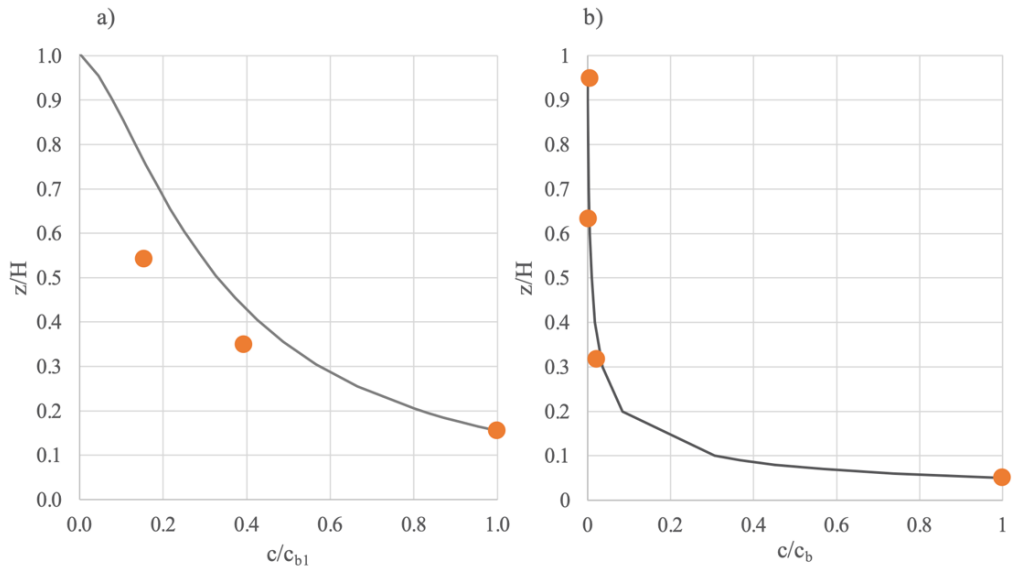

Figure 3.5 Suspended Sediment Data

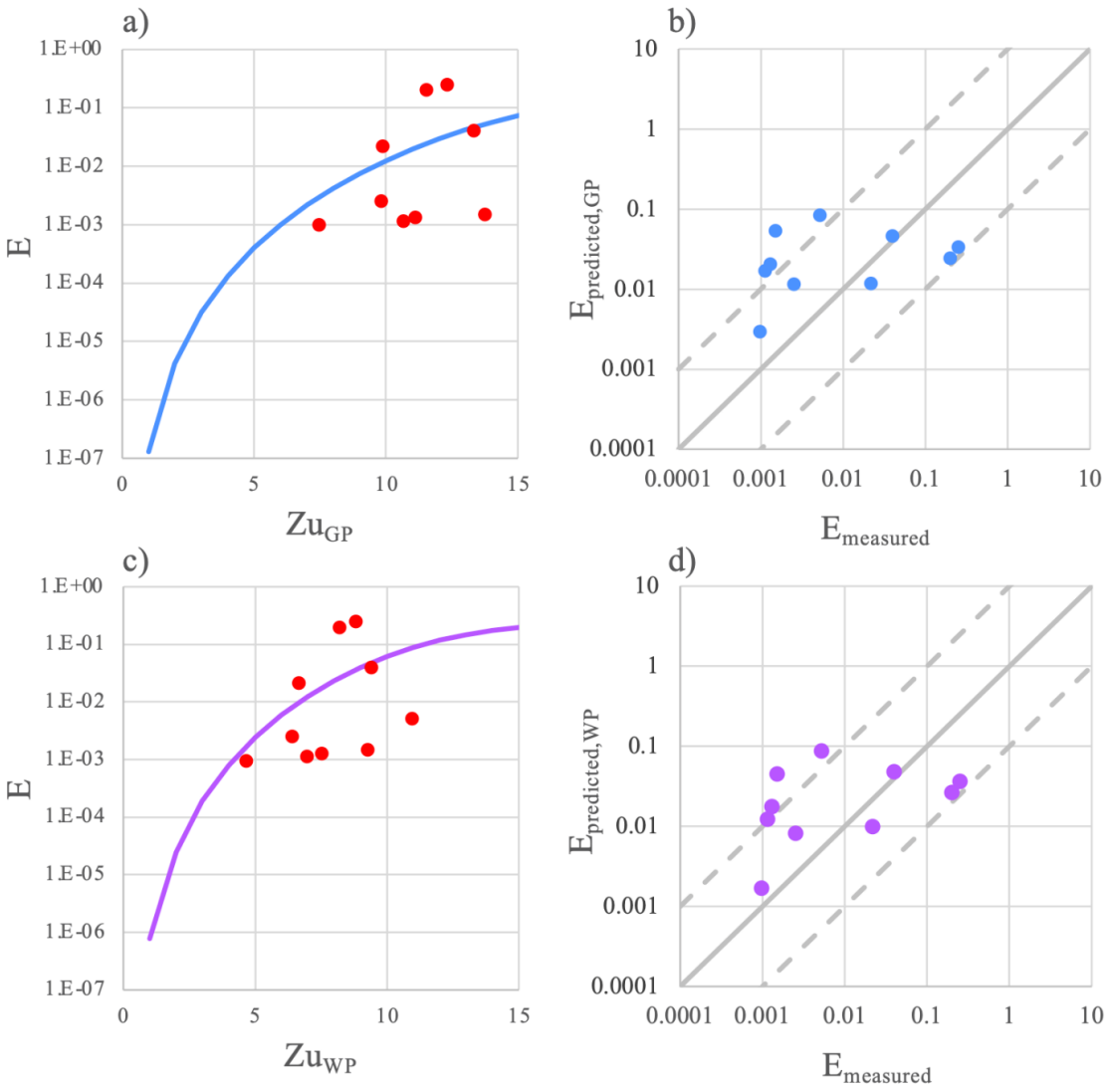

Figure 3.6 Suspended Sediment Entrainment Rates

CHAPTER 4

DISCUSSION

To determine if the behavior of the upper regime bedforms observed in the experiments performed at the University of South Carolina (UofSC) can be generalized, I plotted the data on washed out dunes and upper regime bedforms collected by Guy et al. (1966) and Kennedy (1960) in the same non-dimensional graphs of Figure 3.4.

Kennedy (1960) performed experiments in a 12.19 m and an 18.28 m recirculating flume at California Institute of Technology using sediments with grain sizes of 0.233 mm and 0.549 mm. The experiments were run until the system reached equilibrium, defined as a condition in which the water and bed surface were both parallel to each other and did not change in time.

Guy et al. (1966) performed experiments in a 0.60 m deep, 2.43 m wide, 45.72 m long recirculating flume and the sediment used in the experiments were collected samples from natural riverbeds in the Fort Collins, Colorado, area. The characteristic sediment grain size of the sediment used in the experiments were 0.19 mm, 0.27 mm, 0.28 mm, 0.32 mm, 0.33 mm, 0.45 mm, 0.47 mm, 0.54 mm, and 0.93 mm. Experiments were run until equilibrium conditions were reached, that is when the water surface and the bed surface slope did not change in time.

The experimental data of Guy et al. (1966) and Kennedy (1960) are presented in Figure 4.1 in non-dimensional plots with the same variable of the non-dimensional plots of Figure 3.4. The ratio between the volumetric sediment load and the flow discharge is

on the horizontal axis, the non-dimensional wavelength (λ/D) is on the vertical axis of panel a, the non-dimensional water depth (H/D) is on the vertical axis of panel b and the ratio between the shear velocity and the settling velocity of the sediment (u^*/v_s) is on the vertical axis of panel c. The same symbols of Figures 3.1 and 3.6 are used to characterize the bed configurations. Blue symbols are used to represent the experiments by Guy et al. (1966) and green symbols are used for the experiments by Kennedy (1960).

In the data summary table Guy et al. (1966) did not specify the migration directions of the antidunes. However, in the description of the experimental runs and in the *Glossary of Terms* Guy et al. (1966) describe the antidunes as bedforms that usually migrate upstream. The classification of the bedforms observed by Kennedy (1960) is based on the notes in the dataset describing how the bedforms interacted with the free surface and if they were migrating in the upstream and downstream direction.

As the ratio between the sediment load and the flow discharge (Q_s/Q_w) increases, the bed configuration evolves from lower regime to upper regime. The non-dimensional plots confirm that two transition zones occur with the first one being between the lower regime and upper regime. The second transition zone occurs within the upper regime distinguishing the transitions between downstream and upstream migration directions. The limits of the transition zone between lower regime and upper regime configurations of Figure 4.1 coincide with those of Figure 3.6, that is $0.0003 \leq Q_s/Q_w \leq 0.0007$. As in Figure 3.4, the upper regime region of Figure 4.1 can be split into two parts, as bedforms can either move downstream (in the same direction of the flow) or in the upstream direction. The transition region between downstream migrating bedforms and upstream

migrating bed forms coincides with that of Figure 3.4 with values of Q_s/Q_w between 0.0015 and 0.0032.

Most of the experiments in Figure 4.1 were performed with sediments finer than 0.62 mm, the boundary grain size between experiments with and without significant suspended load. Notably, as Q_s/Q_w increases, all the upstream migrating antidunes become longer (λ/D increases) until they evolve into chute and pools (also known as cyclic steps) when $Q_s/Q_w > 0.01$ (Figure 4.1a). In the UofSC dataset, 6B-SS was the only experimental run that showed beginning stages of cyclic step behavior.

The non-dimensional flow depth (H/D) does not noticeably change with Q_s/Q_w and this is probably due to the lack of experiments with downstream migrating antidunes in the database (Figure 4,1b). The ratio between the shear velocity and the fall velocity of the sediment particles u_*/v_{sg} indicates significant suspension for the experiments with upstream migrating antidunes at high values of Q_s/Q_w and for cyclic steps. Values of u_*/v_{sg} smaller than one is typical of bed configurations classified as transitional, plane or with standing waves.

4.1 Figure Caption

Figure 4.1. Non-dimensional diagrams of Figure 3.4 with the experimental points of the experiments performed by Guy et al. (1966) and Kennedy (1960). a) non-dimensional wavelength (λ/D) versus the ratio between the volumetric sediment load and the flow discharge Q_s/Q_w, b) non-dimensional water depth (H/D) versus Q_s/Q_w, c) ratio between hear velocity and settling velocity u^*/v_{sg} versus Q_s/Q_w,

4.2 Figures

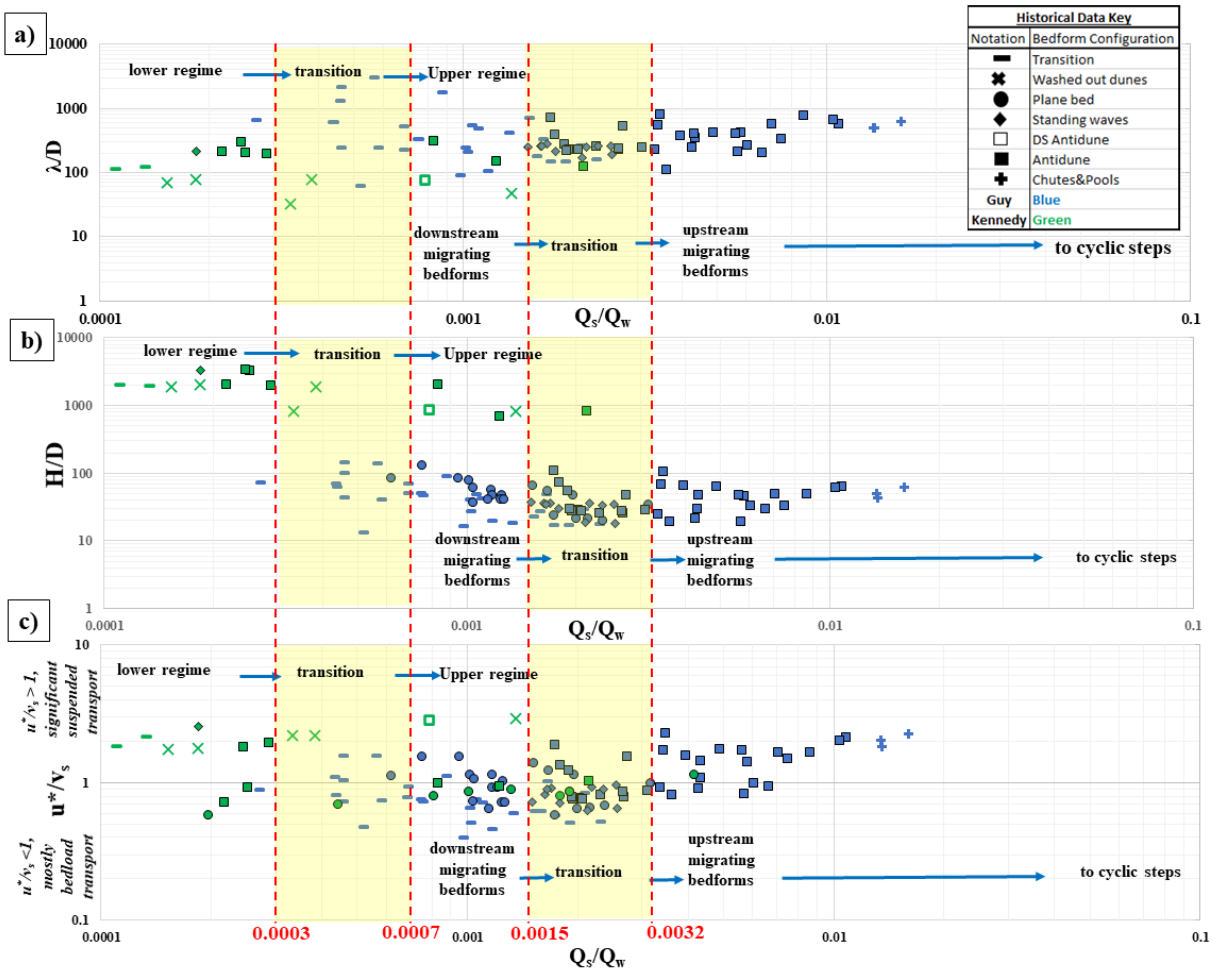

Figure 4.1. Non-dimensional diagrams of Figure 3.4 with the experimental points of the experiments performed by Guy et al. (1966) and Kennedy (1960). a) non-dimensional wavelength (λ/D) versus the ratio between the volumetric sediment load and the flow discharge Q_s/Q_w, b) non-dimensional water depth (H/D) versus Q_s/Q_w, c) ratio between hear velocity and settling velocity u^*/v_{sg} versus Q_s/Q_w,

CHAPTER 5

CONCLUSION

Open channel laboratory experiments were performed in a sediment feed flume to test the hypothesis that grainsize and sediment supply play a significant role on the geometry and type of upper regime bedforms. The flow rate, sediment feed rate, and sediment size were designed to perform experiments with bed material transported as bedload transport and in suspension in the water column, and to reach a bed configuration as close to cyclic steps as possible.

Main results of the experimental result presented in this thesis are:

1) As the ratio between feed rate and flow rate increases, bedforms evolve from lower regime to upper regime configurations. Within the upper regime, antidunes that migrate in the downstream direction are characterized by low values of the ratio Q_s/Q_w. Upstream migrating antidunes and cyclic steps have higher values of Q_s/Q_w than the downstream migrating antidunes.

2) Experimental runs with fine sediment had higher suspended sediment load ($u^*/v_s > 1$), than those that were performed with coarser material. Interestingly, upper regime bedforms developed in experimental runs with significant sediment in suspension.

3) As the flow discharge decreases, the flow depth decreases, and the bed configuration changes.

4) The wavelength of upstream migrating bedforms increases with the ratio between sediment supply and flow discharge.

The experimental data set that is presented almost reaches stable cyclic step bed configurations. It is suggested that further investigation of sediment mixes between 0.1 mm and 0.34 mm with Q_s/Q_wratios greater than 0.01 should be performed.

REFERENCES

Alexander, J., Bridge, J. S., Cheel, R. J., & Leclair, S. F. (2001). Bedforms and associated sedimentary structures formed under supercritical water flows over aggrading sand beds. *Sedimentology*, *48*(1), 133-152. https://onlinelibrary.wiley.com/doi/abs/10.1046/j.1365-3091.2001.00357.x

Alexander, J., & Fielding, C. (1997). Gravel antidunes in the tropical Burdekin River, Queensland, Australia. *Sedimentology*, *44*(2), 327-337. https://onlinelibrary.wiley.com/doi/abs/10.1111/j.1365-3091.1997.tb01527.x

Araya, T., & Masuda, F. (2001). Sedimentary structures of antidunes. An overview. *Journal of the Sedimentological Society of Japan*, *53*(53), 1-15.

Capart, H., & Fraccarollo, L. (2011). Transport layer structure in intense bed-load. *Geophysical Research Letters*, *38*(20). https://agupubs.onlinelibrary.wiley.com/doi/abs/10.1029/2011GL049408

Carling, P. A., & Shvidchenko, A. B. (2002). A consideration of the dune:antidune transition in fine gravel. *Sedimentology*, *49*(6), 1269-1282. https://onlinelibrary.wiley.com/doi/abs/10.1046/j.1365-3091.2002.00496.x

Chiew, Y.-M., & Parker, G. (1994). Incipient sediment motion on non-horizontal slopes. *Journal of Hydraulic Research*, *32*(5), 649-660. https://doi.org/10.1080/00221689409498706

Covault, J. A., Kostic, S., Paull, C. K., Sylvester, Z., & Fildani, A. (2017). Cyclic steps and related supercritical bedforms: Building blocks of deep-water depositional systems, western North America. *Marine Geology*, *393*, 4-20. https://www.sciencedirect.com/science/article/pii/S0025322716303905

Dietrich, W. E. (1982). Settling velocity of natural particles. *Water Resources Research*, *18*(6), 1615-1626. https://agupubs.onlinelibrary.wiley.com/doi/abs/10.1029/WR018i006p01615

Engelund, F. (1970). Instability of erodible beds. *Journal of Fluid Mechanics*, *42*(2), 225-244.

Engelund, F., & Hansen, E. (1967). A monograph on sediment transport in alluvial streams. *Technical University of Denmark 0stervoldgade 10, Copenhagen.*

Froude, M. J., Alexander, J., Barclay, J., & Cole, P. (2017). Interpreting flash flood palaeoflow parameters from antidunes and gravel lenses: An example from Montserrat, West Indies. *Sedimentology, 64*(7), 1817-1845. https://onlinelibrary.wiley.com/doi/abs/10.1111/sed.12375

Garcia, M., & Parker, G. (1991). Entrainment of bed sediment into suspension. *Journal of Hydraulic Engineering, 117*(4), 414-435.

Gilbert, G. K., & Murphy, E. C. (1914). *The transportation of debris by running water*: US Government Printing Office.

Guy, H. P., Simons, D. B., & Richardson, E. V. (1966). *Summary of alluvial channel data from flume experiments, 1956-61*: US Government Printing Office.

Hernandez-Moreira, R., Jafarinik, S., Sanders, S., Kendall, C. G. S. C., Parker, G., & Viparelli, E. (2020). Emplacement of massive deposits by sheet flow. *Sedimentology, 67*(4), 1951-1972. https://onlinelibrary.wiley.com/doi/abs/10.1111/sed.12689

Jafarinik, S., Moreira, R., & Viparelli, E. (2019). Alluvial Morphodynamics of Bedrock Reaches Transporting Mixed-Size Sand. Laboratory Experiments. *Journal of Geophysical Research: Earth Surface, 124*, 3067-3089. https://doi.org/10.1029/2019JF005058

Kennedy, J. F. (1960). *Stationary waves and antidunes in alluvial channels.* California Institute of Technology, PhD Thesis.

Lang, J., Le Heron, D. P., Van den Berg, J. H., & Winsemann, J. (2021). Bedforms and sedimentary structures related to supercritical flows in glacigenic settings. *Sedimentology, 68*(4), 1539-1579. https://onlinelibrary.wiley.com/doi/abs/10.1111/sed.12776

Langford, R., & Bracken, B. (1987). Medano Creek, Colorado, a model for upper-flow-regime fluvial deposition. *Journal of Sedimentary Research, 57*(5), 863-870. https://doi.org/10.1306/212F8C88-2B24-11D7-8648000102C1865D

Moodie, A. J., Nittrouer, J. A., a, H., Carlson, B. N., Wan, Y., Lamb, M., & Parker, G. (2000). Suspended-sediment induced stratification inferred from concentration and velocity profile measurements in the lower Yellow River, China. Accepted manuscript, *Water Resources Research*, 56, e2020WR027192. https://doi.org/10.1029/2020WR027192

Paola, C., Wiele, S., & Reinhart, M. (2006). Upper-regime parallel lamination as a result of turbulent sediment transport and low-amplitude bedforms. *Sedimentology, 36*, 47-59.

Parker, G. (1991). Selective sorting and abrasion of river gravel. II: Applications. *Journal of Hydraulic Engineering, 117*(2), 150-171.

Parker, G. (2004). *1D Sediment Transport Morphodynamics with applications to Rivers and Turbidity Currents*. Copyrighted e-book freely downloadable at http://hydrolab.illinois.edu/people/parkerg/morphodynamics_e-book.htm

Parker, G., & Klingeman, P. C. (1982). On why gravel bed streams are paved. *Water Resources Research, 18*(5), 1409-1423.

Pickup, G., Ringrose, P., Jensen, J., & Sorbie, K. (1994). Permeability tensors for sedimentary structures. *Mathematical Geology, 26*, 227-250.

Simons, D. B., & Richardson, E. V. (1966). *Resistance to flow in alluvial channels*: US Government Printing Office.

Smillie, Z., Stow, D., & Esentia, I. (2019). Deep-Sea Contourites Drifts, Erosional Features and Bedforms. In J. K. Cochran, H. J. Bokuniewicz, & P. L. Yager (Eds.), *Encyclopedia of Ocean Sciences (Third Edition)* (pp. 97-110). Oxford: Academic Press.

Turowski, J. M., Rickenmann, D., & Dadson, S. J. (2010). The partitioning of the total sediment load of a river into suspended load and bedload: a review of empirical data. *Sedimentology, 57*(4), 1126-1146.

Vanoni, V. A. (1974). Factors determining bed forms of alluvial streams. *Journal of the Hydraulics Division, 100*(3), 363-377.

Vanoni, V. A. (2006). *Sedimentation Engineering: Classic Edition*. Reston, United States: American Society of Civil Engineers.

Vanoni, V. A., & Brooks, N. H. (1957). *Laboratory studies of the roughness and suspended load of alluvial streams*: US Army Engineer Division, Missouri River.

Vesipa, R., Camporeale, C., & Ridolfi, L. (2012). A shallow-water theory of river bedforms in supercritical conditions. *Physics of Fluids, 24*(9), 094104.

Viparelli, E., Solari, L., & Hill, K. (2015). Downstream lightening and upward heavying: Experiments with sediments differing in density. *Sedimentology, 62*(5), 1384-1407.

Wright, S., & Parker, G. (2004). Density stratification effects in sand-bed rivers. *Journal of Hydraulic Engineering, 130*(8), 783-795.

Yang, J. Q., & Nepf, H. M. (2019). Impact of Vegetation on Bed Load Transport Rate and Bedform Characteristics. *Water Resources Research*, *55*(7), 6109-6124. https://agupubs.onlinelibrary.wiley.com/doi/abs/10.1029/2018WR024404

Yokokawa, M., Hasegawa, K., Kanbayashi, S., & Endo, N. (2010). Formative conditions and sedimentary structures of sandy 3D antidunes: an application of the gravel step-pool model to fine-grained sand in an experimental flume. *Earth Surface Processes and Landforms*, *35*(14), 1720-1729. https://onlinelibrary.wiley.com/doi/abs/10.1002/esp.2069